



HAL
open science

Three-dimensional investigation of fragment distribution in Al -7 wt.% Si solidified in microgravity

L. Abou-Khalil, Z. Thompson, Guillaume Reinhart, T. Stan, L. Sturz, G. Zimmermann, P.W. Voorhees, Nathalie Mangelinck-Noël, H. Nguyen-Thi

► To cite this version:

L. Abou-Khalil, Z. Thompson, Guillaume Reinhart, T. Stan, L. Sturz, et al.. Three-dimensional investigation of fragment distribution in Al -7 wt.% Si solidified in microgravity. *Acta Materialia*, 2023, 250, pp.118882. 10.1016/j.actamat.2023.118882 . hal-04101354

HAL Id: hal-04101354

<https://amu.hal.science/hal-04101354v1>

Submitted on 19 May 2023

HAL is a multi-disciplinary open access archive for the deposit and dissemination of scientific research documents, whether they are published or not. The documents may come from teaching and research institutions in France or abroad, or from public or private research centers.

L'archive ouverte pluridisciplinaire **HAL**, est destinée au dépôt et à la diffusion de documents scientifiques de niveau recherche, publiés ou non, émanant des établissements d'enseignement et de recherche français ou étrangers, des laboratoires publics ou privés.

Three-dimensional investigation of fragment distribution in Al – 7 wt.% Si solidified in microgravity

**L. Abou-Khalil^{1,*}, Z. Thompson², G. Reinhart¹, T. Stan², L. Sturz³, G. Zimmermann³,
P. W. Voorhees², N. Mangelinck-Noël¹, H. Nguyen-Thi¹**

¹ Aix Marseille Univ, Université de Toulon, CNRS, IM2NP, Marseille, France

² Department of Materials Science and Engineering, Northwestern University, Evanston, USA

³ Access e.V, Intzestrasse 5, 52072, Aachen, Germany

Abstract

Three-dimensional (3D) reconstruction of the microstructure of Al – 7 wt.% Si samples solidified in microgravity conditions on board of the International Space Station was obtained from serial-sectioning images. The main objective was to quantify the number of dendrite fragments issued from the solidification process in absence of buoyancy force and with motionless dendrite fragments on contrary to ground-based experiments. The results show that the number of fragments strongly depends on the dendrite network configuration. More fragments are observed in the sample containing several dendrites with different orientations compared to a sample with well-aligned dendrites. . Moreover, it has been found that the highest number of fragments is mainly located in the region corresponding to an incipient grain boundary where dendrites with different orientations compete. Indeed, in this region solute accumulates and the microstructure is finer which is more prone to fragmentation of dendritic arms growing in this region. Thus, a mechanism that leads to the formation of dendrite fragmentation is identified: dendrite misorientation during solidification.

* Corresponding author at Aix Marseille Univ, Université de Toulon, CNRS, IM2NP, 13397, Marseille, France; Email address: lara.aboukhalil@im2np.fr

Keywords: Solidification, Fragmentation, Microgravity, 3D reconstruction, Dendrite orientation, Dendrite growth competition.

1. Introduction

Dendrite fragmentation is one of the most important phenomena that occurs during the formation of the solidification microstructures of metal alloys. Fragmentation is the process of detachment of secondary or tertiary dendrite arms from the trunk and it is the most potent mechanism for the promotion of CET (Columnar-to-Equiaxed Transition) in non-refined alloys [1,2]. A deep understanding of the conditions for fragmentation is still an open question and not yet fully clear. Different mechanisms have been identified as potential reasons for the detachment of fragments, such as local remelting caused by: (i) solute pileup in the mushy zone [3] or (ii) the release of latent heat from the solidification of interdendritic melt [4] and (iii) coarsening process (induced by Gibbs-Thomson effect) [5]. Furthermore, gravity-driven phenomena can be an additional effect for promoting fragmentation due to buoyant forces [2]. The two main gravity-driven phenomena are (i) natural convection in the liquid in the close vicinity of dendrite tips that can induce remelting at the neck of the secondary arm and (ii) buoyancy force that acts on dendrite arms leading to mechanical effects such as secondary arm bending [6] and in some cases arm detachment [6–8]. Fragmentation can also be induced by forced melt flow. In a model alloy dendritic fragmentation was increased by higher flow velocity [9]. Directional solidification experiments with Accelerated Crucible Rotation Technique revealed that forced convection significantly increased the probability of detachment and transport of fragments in Al - 7 wt% Si alloy [10]. Additionally, experiments with forced melt flow induced by electromagnetic stirring

demonstrated enhanced fragmentation. This effect was also explained by a modified dendrite fragmentation criterion [11].

It is therefore timely to separate the effects at the origin of fragmentation with the objective to further understand the fragmentation mechanism. A way to eliminate or reduce gravity effects on microstructure formation is to perform experiments in microgravity environment so that natural convection, buoyancy force, hydrostatic pressure and mechanical effects become negligible [12]. Benchmark data are obtained by this means, allowing a sound comparison with theoretical models or numerical simulations [13–16]. Comparison between solidification experiments carried out on Earth and in microgravity underlined the major impact of gravity on the fragmentation phenomenon, as well as on the movement of fragments after their detachment [17]. Salloum-Abou-Jaoude *et al.* [17] showed that the number of fragmentation events is much larger in normal gravity than in microgravity conditions.

In the framework of the CETSOL (Columnar to Equiaxed Transition in SOLidification processes) project from the European Space Agency (ESA), solidification experiments were carried out on Al-7wt% Si alloy (refined or non-refined) on-board of the International Space Station (ISS) in the Materials Science Laboratory (MSL). The analysis of those experiments has been up to now limited to 2D characterization on longitudinal sections and cross sections [12,18–20]. For deeper examination and analysis of the dendrite fragments, grain structure characteristics and segregation distribution, 3D characterizations are requested.

With the development of third-generation synchrotron radiation X-ray sources, X-ray tomography has become a popular technique to reveal in 3D the microstructure phases and morphologies of metal alloys. The main advantage of X-ray tomography is that it is a non-destructive technique that allows in-situ experiments [21]. Several mechanisms were captured

during 4D synchrotron X-ray tomographic imaging such as interface instability and dendrite fragmentation and the quantitative results were compared to proposed mechanisms [8]. However, the limited access to synchrotron sources is a significant drawback. The use of laboratory X-ray tomography devices is also useful to obtain post-mortem reconstructions of samples [22], but the field-of-view is usually restricted when using a high spatial resolution. Additionally, almost no contrast is expected in the particular case of Al-7wt% Si alloys as the contrast comes mainly from density differences in this technique.

Another technique to characterize the dendrite morphology in 3D is the serial-sectioning process, which is a post-mortem method. It has been described in detail in [23] and allows reconstructing large volumes with a very good spatial resolution. For instance, the reconstructed microstructure in a Pb-Sn alloy [24] gave the opportunity to measure the interfacial curvature. From these results, a snapshot of the spatial distribution of the mean curvature was determined and from this the diffusion fluxes that are at the core of the coarsening process. T. Cool and P. W. Voorhees [25] performed isothermal coarsening experiments in microgravity conditions to focus on capillary driven fragmentation alone. Indeed, in these conditions, the natural convection, the buoyancy force and the mechanical effects become negligible. The morphology of the structure and the number of fragments were determined using three-dimensional reconstructions. After studying the evolution of secondary dendrite arms during isothermal, interfacial energy-driven coarsening, the dendrites that were measured experimentally in microgravity experiments were used as an initial condition in a phase-field simulation.

The subject of the present work is the study of fragment distribution in bulk samples after directional solidification of Al - 7 wt.% Si alloys carried out on board ISS. 3D characterization using serial-sectioning technique was used. Qualitative and quantitative analysis of the

microstructure was performed. Using the 3D reconstructions, the dendrite orientations with respect to the temperature gradient were determined and the fragment number was quantified. The effect of the dendrite growth competition on fragmentation is then discussed in detail. Qualitative and quantitative benchmark data needed for a sound comparison with theoretical models or numerical simulations are provided by the microgravity conditions and by the use of 3D reconstruction.

2. Methods and materials

2.1. Microgravity experiments

The samples analyzed in this paper were obtained from experiments that took place onboard the International Space Station (ISS) in the Microgravity Science Laboratory (MSL) using a Bridgman-type Solidification and Quenching Furnace (SQF) which was described in detail in our previous studies [19]. The SQF furnace consists of a cold zone with a Liquid Metal Ring (LMR), a hot zone equipped with four heaters that can be adjusted independently to achieve the required temperature gradient along the sample main axis and of an additional device that allows the application of a Rotating Magnetic Field (RMF) during solidification. Solidification of the alloy is performed by the controlled displacement of the furnace relatively to the fixed sample cartridge assembly (SCA) at a chosen velocity which can be varied during the experiment, and/or by applying a cooling rate on the hot zone.

The metal alloy sample has a cylindrical shape with 8 mm in diameter and 245 mm in length. It is mounted inside an Al_2O_3 tube crucible together with Shapal plugs at both ends. Twelve thermocouples, evenly spaced by 20 mm, are located in four machined external grooves at the outer surface of the crucible to record the temperature profile.

Al – 7 wt.% Si grain refined and non-grain refined alloys provided by Hydro Aluminum Rolled Products GmbH were used in this work. 0.5 wt.% of master alloy AlTi5B was added for the grain refinement. The solidification of the grain refined alloy was carried out during the experiment labelled FM1, and the solidification of the non-refined alloy was carried out during the experiment labelled FM2. The samples were solidified in three successive stages.

- Stage I: the objective of this stage is to achieve a steady-state columnar growth in diffusive conditions, with no RMF (Rotating Magnetic Field). Accordingly, the initial temperature gradient (G) is about 4 K/mm and the solidification is initiated by the pulling of the furnace at a velocity $v_1 = 0.02$ mm/s.
- Stage II: a simultaneous sudden jump of the pulling velocity from $v_1 = 0.02$ mm/s to $v_2 = 0.2$ mm/s and a cooling down of the hot zone at a rate $R = 0.133$ K/s is applied with the objective to trigger the columnar to equiaxed transition. In addition, for FM2, the RMF was turned on with frequency $f = 57$ Hz and magnetic field strength of $B = 0.5$ mT during the whole duration of stage II to induce a forced melt flow.
- Stage III: the quenching of the sample induced by a fast furnace pulling is applied to complete the solidification. During this final quenching stage, the temperature gradient and cooling rates are no longer controlled, but the temperature profile is still recorded.

The evolution of the grain structure and the CET were studied in our previous work [19]. The analysis presented in this work concerns only the parts solidified during Stage I. The solidification microstructures along longitudinal sections of FM1 and FM2 are presented in Figure 1. The sections were electrolytically etched and observed in a polarization microscope. The different colors correspond to grains with different crystallographic orientation. The initial seeds appear on the left side of Figure 1. Solidification starts from the seeds. Under the solidification conditions of

stage I, a columnar structure is obtained toward the right-hand side of the image in the direction of the temperature gradient. An advanced three-dimensional analysis based on serial-sectioning was used to investigate the origin of dendrite fragmentation.

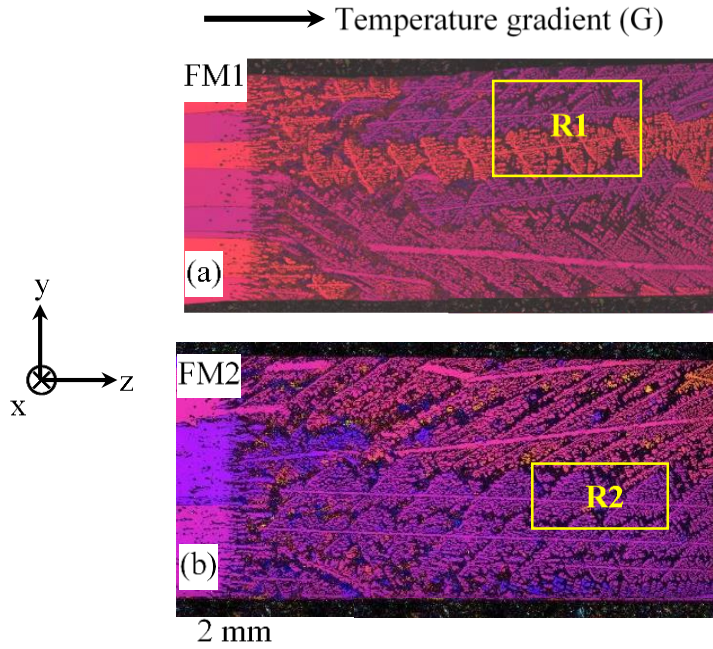


Figure 1: Solidification microstructures obtained with optical microscope for FM1 and FM2 experiments solidified during the stage I. The yellow frames (boxes) indicate the regions of three-dimensional analysis. The solidification direction and the temperature gradient is along z direction.

2.2. Serial-sectioning and segmentation

Three-dimensional reconstructions of FM1 and FM2 microstructures were performed by serial-sectioning at Northwestern University. Selected areas of interest are highlighted by the yellow frames in Figure 1. The areas R1 and R2 correspond to regions that were solidified during stage I of the FM1 and FM2 experiments, respectively. The temperature gradient ahead of the liquidus isotherm G_L and the velocity of the liquidus isotherm v_L for R1 and R2 were calculated using the method mentioned in [12] based on the analysis of the recorded temperature profiles (Table I).

Table I: Table comparing the processing parameters for R1 and R2.

Parameters	R1	R2
G (K/mm)	4.6	4.8
V (mm/s)	0.017	0.016

Parts of few mm in width (y) and length (z) (cf. Table II) and 1.6 mm in thickness (x) were cut from the original samples and mounted into a LEICA automated serial-sectioner. At each step, approximately 4 μm in depth was removed by a rotating diamond blade after which, an optical micrograph of the new sample surface was captured. This process was repeated until a sufficient number of images was obtained to be able to reconstruct a 3D volume of the microstructure [23]. The pixel sizes for each reconstruction are also shown in Table II.

Table II: Table showing the dimensions of the 3D-reconstructed regions (R1 refined alloy and R2 non-refined alloy) and the pixel size.

	R1	R2
Dimension (mm)		
width \times length \times thickness	$3.1 \times 4.8 \times 1.6$	$2.1 \times 4.4 \times 1.5$
Pixel size (μm)		
width \times length \times thickness	$2.09 \times 2.09 \times 4.05$	$1.65 \times 1.65 \times 3.62$

The resulting image sections were smoothed using a median filter in the direction perpendicular to the slicing direction to ensure the removal of artifacts. These median-filtered image stacks were then segmented into dendrite and background eutectic phases using a modified version of the Expectation-Maximization/Maximization of the Posterior Marginals (EM/MPM) software [26,27].

To identify the number of independent bodies within 3D datasets, modifications were added to the EM/MPM software including a channeling algorithm to increase the number of narrow channels between dendrite bodies during segmentation [27]. Further adjustments to the

segmentation were made, including morphological opening or changes by hand using an editing software such as GIMP (GNU Image Manipulation Program). The segmented images were used to analyze and characterize the independent bodies as described in the following sections.

3. Results

3.1. Characterization of the connected dendrite groups

To identify and count the non-connected bodies in each sample, the “3D Object Counter” plugin of ImageJ software [28] was used. This plugin counts and displays the number of 3D objects in a volume. In the non-refined alloy region (R2), three main separated large bodies are found with a volume between 1055 and 1074 μm^3 . These three bodies are presented in Figure 2b with different colors (blue, green and yellow) and correspond to dendritic microstructures. The same method was applied for the grain refined alloy region (R1). In R1, four main separated large bodies with a volume between 1893 and 1928 μm^3 are found and presented in Figure 2a with different colors (yellow, blue, green and magenta).

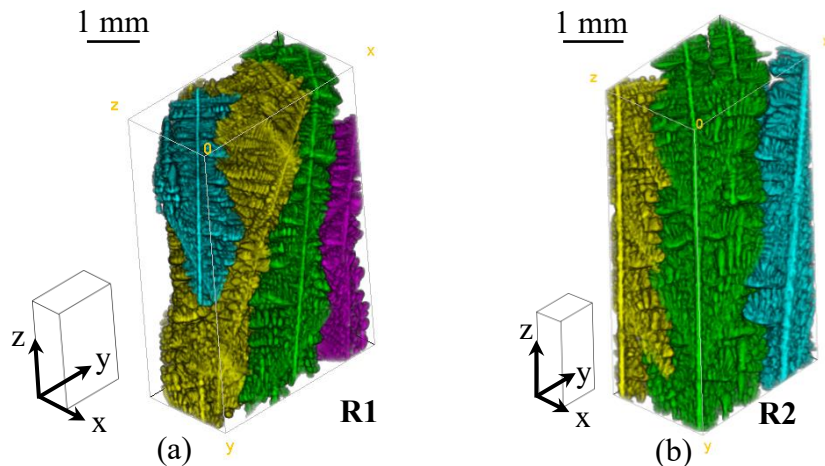


Figure 2: The 3D microstructure reconstruction for (a) R1 and (b) R2, showing the different bodies (connected dendrites groups) represented with different colors.

The volume-to-surface area ratio Sv^{-1} , which is the ratio of the dendrite volume divided by the dendrite surface area, was calculated to measure the characteristic dimensions of the microstructure for each sample. The Sv^{-1} has been chosen over the more traditional secondary dendrite arm spacing (SDAS) for two reasons. First, it can be computed for non-dendritic microstructures, allowing comparisons to other regions or datasets lacking dendrites. Second, it is more objective and easier to measure accurately using 3D data than secondary dendrite arm spacing (SDAS). The Sv^{-1} of the microstructure for the whole 3D volume of the non-refined alloy (R2) is $14.1 \mu\text{m}$. The Sv^{-1} values of each dendrite group are $14.1 \mu\text{m}$, $14.0 \mu\text{m}$ and $14.4 \mu\text{m}$ for the yellow, green and blue bodies, respectively. The Sv^{-1} of the microstructure for the whole 3D volume in the refined alloy (R1) is $14.3 \mu\text{m}$. The Sv^{-1} values of each group are $13.9 \mu\text{m}$, $13.2 \mu\text{m}$, 14.7 and $14.0 \mu\text{m}$ for the yellow, cyan, magenta and green bodies, respectively.

To characterize the different orientation of the dendrites in each body, projections were done along the growth directions of various dendrite arms. Typical projections are shown in Figure 3. For the non-refined alloy (R2), the projection presented in Figure 3b₁ clearly shows that all the dendrites forming the yellow and green bodies are parallel to each other. However, the $\langle 100 \rangle$ directions of the dendrites forming the blue one are misoriented with respect to the orientation of the green and yellow dendrites. Therefore, two different dendrite orientations are present and noted A and B. Similarly, according to the projection of the refined alloy (R1) presented in Figure 3a₁, four different dendrite orientations are found, noted A', B', C' and D'. It is worth noting that dendrites in the same connected body are not necessarily all parallel, as visible for the yellow and green ones in Figure 3a₁ where two dendrite orientations co-exist: A' and B', A' and C' for the yellow and green bodies, respectively.

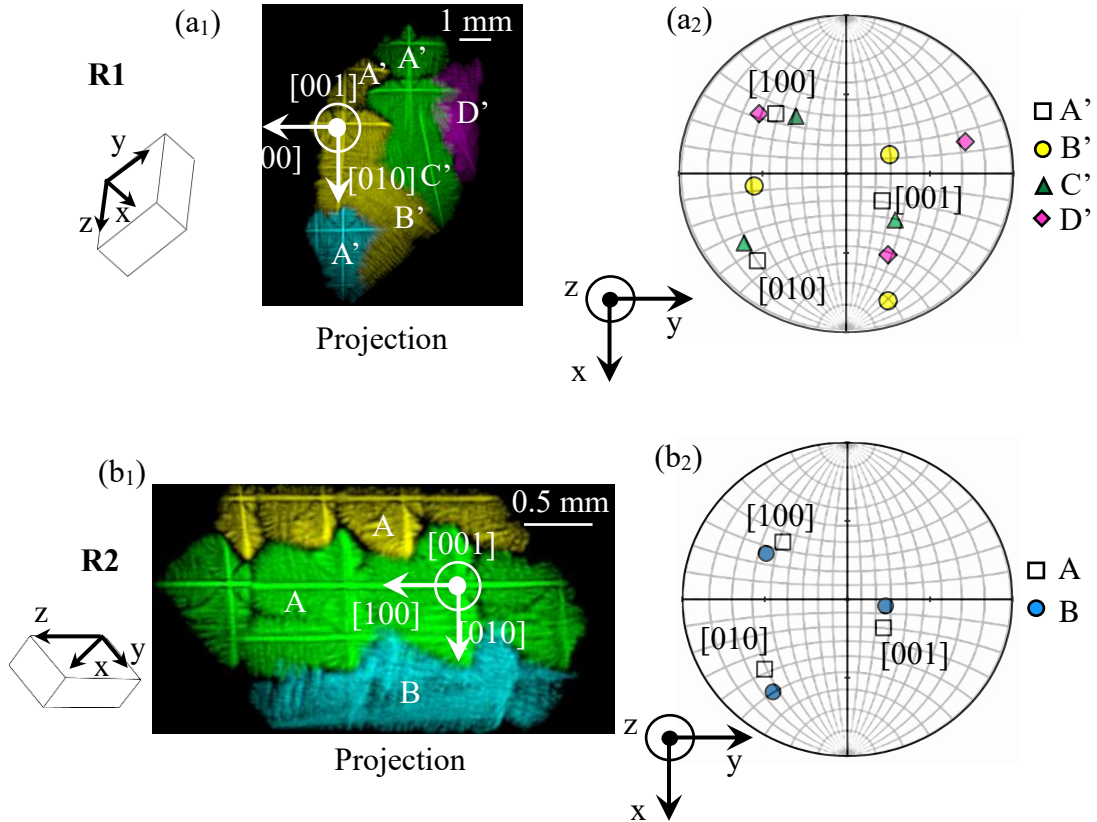


Figure 3: (a1) Projection of the dendritic microstructure in R1 showing the four dendrite orientations in the sample. (a2) The reconstructed pole figure showing the dendrite orientations in R1 with respect to the temperature gradient (G).

(b1) Projection of the dendritic microstructure in R2 showing the two dendrite orientations in the sample. (b2) The reconstructed pole figure showing the dendrite orientations in R2 with respect to the temperature gradient (G).

An additional analysis was done to characterize the dendrite orientations with respect to the temperature gradient (G) direction. Based on the observation of crosses corresponding to perpendicular dendrite arms in the projections of Figure 3, it was assumed that the dendrite arms are developing along $\langle 100 \rangle$ directions. Three orthogonal axes were drawn following dendrite arms developing in the direction of the temperature gradient for each different dendrite orientation. The projection along the temperature gradient direction of these three axes was then used to deduce corresponding pole figures. By this means, it is possible to get information on the crystallographic orientation of the dendrites with an accuracy of $\pm 5^\circ$ in measurement. For example, Figure 3b2

represents the pole figure with the two dendrite orientations present in the non-refined alloy (R2). The orientations A and B are only slightly misoriented. The primary trunks of the green and yellow dendrites (orientation A) both form an angle of $\sim 30^\circ$ with respect to the temperature gradient, while the primary trunk of the blue dendrite group (orientation B) form an angle of $\sim 26.5^\circ$ with the temperature gradient. Figure 3a₂ represents the pole figure with the four dendrite orientations present in the refined alloy (R1). It can be seen that:

- The primary trunks of the dendrites with the main orientation A' form an angle of $\sim 30^\circ$ with respect to the temperature gradient.
- The primary trunk of the dendrites with the orientation B' also forms an angle of $\sim 30^\circ$ with respect to the temperature gradient, but they form an angle of $\sim 60^\circ$ with respect to orientation A'.
- The primary trunks of the dendrites with the orientations C' and D' form a larger angle with respect to the temperature gradient (~ 44 and 41° respectively).

The details of the angles between the dendrite arms and the temperature gradient are gathered in Table III.

Table III: Table showing the orientations with respect to the temperature gradient orientation in R1 and R2.

Sample	Orientation	Primary trunk angle	Secondary arm angles	
Refined alloy (R1)	A'	30.8°	71.3°	53.8°
	B'	31.8°	78.7°	58.0°
	C'	44.2°	73.7°	45.0°
	D'	41.6°	72.9°	58.3°
Non-refined alloy (R2)	A	30.6°	66.9°	53.7°
	B	26.5°	67.1°	59.4°

3.2. Fragment identification and counting

After the characterization of the dendrite bodies and of their orientation in each sample, the next step was the determination of the fragment density. To find an accurate value, a proper minimum cutoff volume needed to be utilized to ensure that small segmentation errors did not inflate the fragment density while also ensuring as many real fragments as possible were counted. To find this minimum volume, 100 bodies were selected randomly from two different samples after running the channeling algorithm. For each of these bodies, a 3D video was analyzed to determine if it was a real body (such as a fragment, sidearm, or full dendrite) or a segmentation error. When organized by volume in voxels, there was a critical volume separating real bodies from errors; however, this value was different for the two samples. This discrepancy between samples also existed when volume was calculated in μm^3 . However, when normalized using $(Sv^{-1})^3$, both samples had a delineation between real bodies and errors at $(1.5 \times Sv^{-1})^3$. Consequently, this value was defined as a critical volume. Above this value, isolated bodies can be considered as fragments not corresponding to segmentation errors. The critical volumes are thus: $21.5 \mu\text{m}^3$ and $21.2 \mu\text{m}^3$ for the R2 and R1, respectively.

Bodies near the edges of the sample boxes can be difficult to correctly identify as they may be connected to another body outside of the sample volume. However, simply removing all bodies touching an edge statistically leads to an undercount of the actual number of fragments present in the sample. To mitigate these edge effects on our counting statistics, the following method was applied. First a copy of each serial-sectioned volume was created. In the copied dataset, primary dendrite bodies were removed. Then, boundaries inside each sample volume were established by moving one voxel inward from each edge until no voxels from any bodies that were touching the original sample boundary were included. This was done in place of a traditional stereographical

test-frame as the independent bodies being analyzed were still much smaller than the size of the new box and not spherically isotropic [29]. Each body that was at least partially contained within the temporary bounding box and not touching the edge of the original sample box was replaced by its centroid. If a centroid was inside the new bounding box, it was included as part of the independent body count. This number of bodies was divided by the volume of the new bounding box to determine the body density in a manner that is less biased by edge effects [30]. The results are as follow and presented in Table IV: in R1, the number of fragments is 106 with a density of 2.5×10^{-8} fragments/ μm^3 . For R2, the number of fragments is 84 with a density of 1.6×10^{-8} fragments/ μm^3 . Thus, the density of fragments in R1 is higher by 1.5 than in R2.

Table IV: Table showing the number of fragments and their densities in the R1 and R2.

	R1	R2
Number of fragments	106	84
Density of fragments (fragments/ μm^3)	2.5×10^{-8}	1.6×10^{-8}

3.3. Fragment attribution to connected dendrite bodies

After the characterization of the connected dendrite bodies and of the number of fragments, image processing was done to attribute the fragments to the different connected dendrites bodies. It allowed determining from which structure they detached. To do so, envelopes were created by applying successive 3D morphological dilation operations to the binarized images of the different dendrite bodies, thus gradually enlarging their boundaries. The dilation process was stopped when the boundaries of the different groups met. Figure 4b and 5b show the envelopes obtained for each dendrite body in R1 and R2. Then, the fragments were attributed to a dendrite group if they fell into the corresponding envelope. It is worth noting that this kind of analysis is possible only

because the samples were solidified in microgravity conditions, so the absence of buoyancy force and convection flow did not induce fragment motion after their detachment.

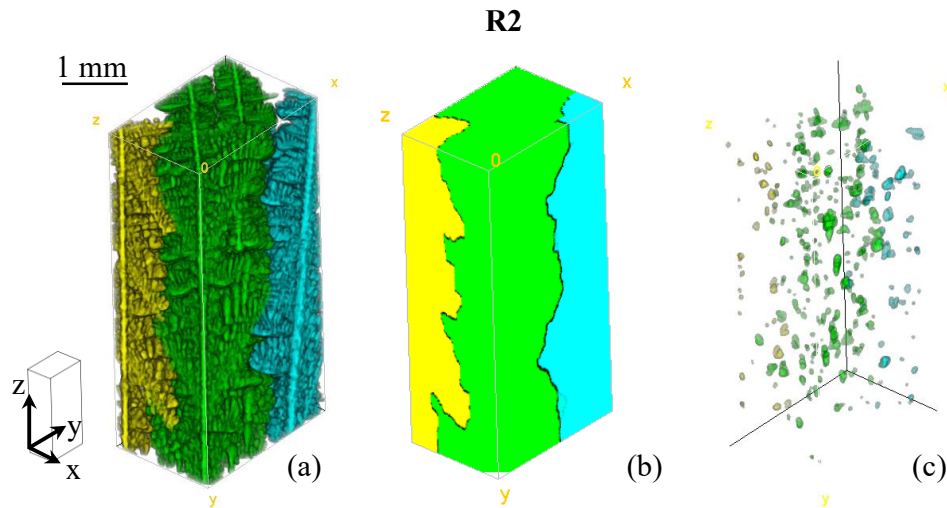


Figure 4: Image showing (a) the three dendrite groups in the R2, (b) their envelopes and (c) their corresponding fragments (according to colors).

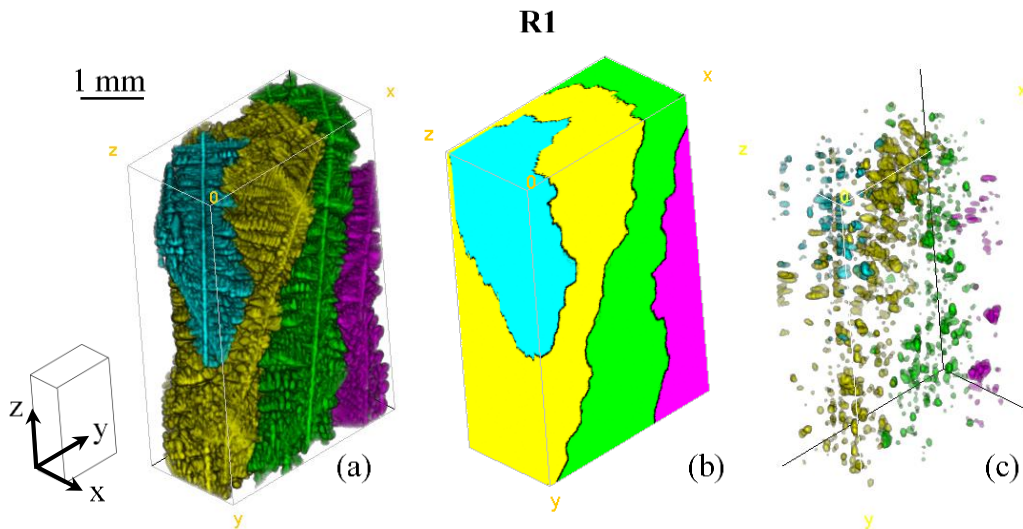


Figure 5: Image showing (a) the four connected dendrite bodies in R1, (b) their envelopes and (c) their corresponding fragments (according to colors).

The fragment distributions with colors corresponding to their attributed dendrite group are shown in Figure 4 and Figure 5. The distribution of the fragments in R2 is rather homogenous, while it is significantly inhomogeneous in R1. Most of the fragments in R1 are present in the upper

part where different dendrite orientations co-exist (A', B' and C'). More specifically, the yellow dendrite group with the orientation C' has the highest number of fragments.

4. Discussion

In this study, advanced characterization in three-dimension by serial-sectioning has been used to analyze the solidification microstructure obtained during microgravity experiments at low growth velocity. The results show that the microstructure consists mainly of large columnar grains with few different orientations, 2 in the investigated volume of the non-refined sample (R2) and 4 in the investigated volume of the refined alloy (R1). The origin of the presence of more dendrite orientations, and therefore of more grains, in R1 is not related to the presence of refiners. Indeed, the samples were solidified at a low growth velocity $v = 0.02$ mm/s for which the refining particles should not be active [18]. In addition, both samples were solidified from solid seeds containing grains with several crystallographic orientations (Fig. 1). Thus, the difference in number of dendrite orientations between R1 and R2 is most likely due to the competition between dendrites from the seeds and to the specific location in the sample that was chosen for the 3D reconstructed volumes.

Another difference between the two regions is the difference in fragment density: the density of fragments in R1 is a factor of 1.5 higher than in the R2. In microgravity, the main reason for fragmentation during solidification could be the coarsening phenomenon occurring while the microstructure is in a mushy state, because the effects of gravity such as buoyancy and fluid flow are neglected [31].

Based on the temperature profile, the time necessary for the R1 and R2 volumes to change from a fully mushy state to a fully solid state were determined. According to these measurements,

it was deduced that the R2 volume stayed a longer time in a mushy state (4.5 min) than the R1 volume (3 min). We chose to focus on these values and not time for the complete solidification, because during this phase (from fully mushy to fully solid state) the microstructure is already formed and surrounded by the liquid so that it is more susceptible to fragmentation. Therefore, if coarsening was at the origin of the difference in the fragment density, the later should be higher in the R2 compared to R1 [31], which is not the case. Thus, additional phenomena must be considered to explain this significant difference in fragment density.

The highest fragment density is found in the upper part of the volume R1 (Fig. 5c). Several cross sections from the bottom to the top of this volume are presented in Figure 6. It shows that the number of fragments (in red) increases from the bottom to the top. Moreover, the fragments are preferentially localized at the encounter between dendrites with different orientations. Specifically, the yellow dendrite with the orientation B' is surrounded by two dendrites with different orientations and is the most fragmented. This points towards the fact that the growth competition between dendrites of different orientation is the dominant phenomenon to explain the fragmentation phenomenon in the present case.

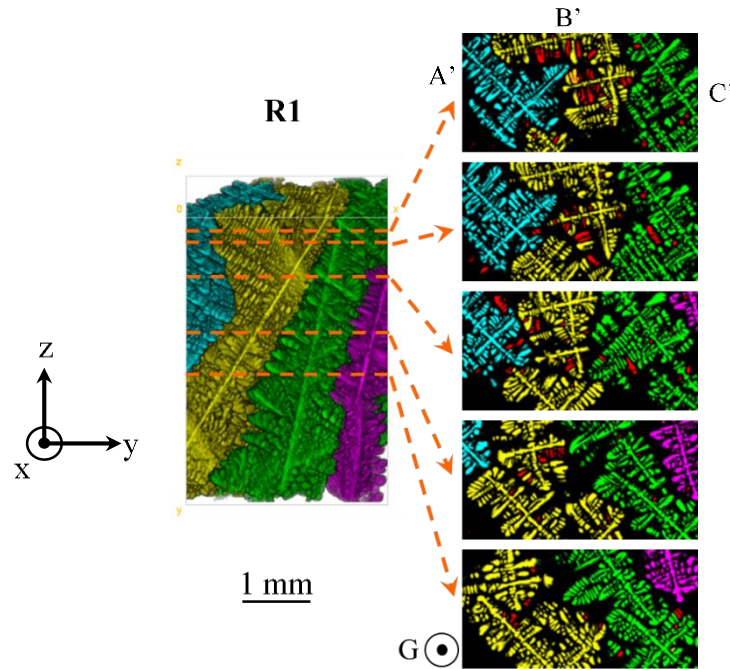


Figure 6: Image showing cross sections of R1 along the growth direction that illustrate the secondary arm competition at the level of grain boundaries. The fragments are highlighted in red.

The competitive growth of dendrites with different orientations leads to an accumulation of solute in the inter-dendritic liquid due to the overlap of their respective solute layers. This has been shown for instance by Takaki *et al.* [32] who studied in three-dimensions the competitive growth of dendrites at converging grain boundaries. Composition measurements could not be performed in our experiments due to the destructive nature of the serial-sectioning procedure. However, the eutectic fraction is expected to increase in regions solidified at higher concentration and can therefore be used to obtain information on solute segregation. Figure 7a shows the evolution of the eutectic fraction measured from the segmented images of volume R1. The amount of eutectic phase is higher than the expected value by ~20% because this region is of local enhanced segregation. Such regions have been previously characterized on the whole longitudinal 2D section in the same sample [19]. A sharp increase in eutectic fraction is observed where the fragment density increases (Fig. 7b and c). It is worth mentioning that the increase in the fragment fraction of R1 (between 0

and 1 mm in Fig. 7b) is due to the presence of fragments bigger in size compared to the others and not to a higher fragment density. This sharp increase in eutectic fraction is at the same level at which the dendrite with the highest relative misorientation (B') intersects with the other dendrites. This confirms that segregation occurred in this region containing misoriented grains.

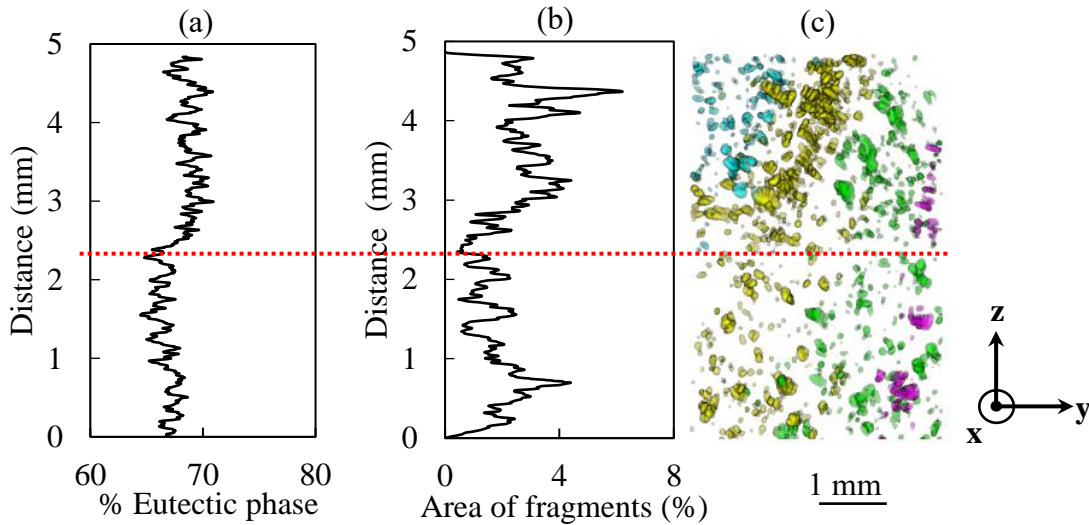


Figure 7: (a) and (b) Graphs showing the percentage of the eutectic phase and the fragments phase along the sample R1. (c) Image showing the fragments in R1. The sharp increase of the percentage of the eutectic phase corresponds to the position where the fragment density increases.

In addition, the Sv^{-1} of the upper part of the yellow dendrite body containing the dendrite with orientation B' has a value of $13.0 \mu\text{m}$ making it the region with the smallest microstructure of the reconstructed volume. This measurement confirms that the dendrite with orientation B' developed in an environment enriched in solute, because segregation modifies the dendrite arm development by decreasing the arm spacing [33] leading to a thinner microstructure. The thinness of the dendrites explains the high number of fragments in this region. Indeed, the pinch-off (detachment) of dendrite arms is favored by low spacing and by finer structure, as recently highlighted by Neumann-Heyme *et al.* [34] using phase-field simulations. This is clearly visible for instance in Figure 7 showing the concomitant increase in eutectic fraction and fragment number in the region containing dendrites with significant misorientations. Thus, the present results obtained in

microgravity conditions illustrate that the competition of dendrites with different crystallographic orientations that leads to grain boundaries in the solid-state and the associated solute segregation can lead to the formation of thinner microstructures and to a higher probability of fragmentations without the interaction of fluid flow and of buoyancy forces.

The microgravity environment allows the detection of the fragments in 3D at their initial position and shows that the fragmentation is enhanced in regions of dendrite growth competition. However, fragmentation is not sufficient to conduct to CET. Gravity effects or fluid flow to transport the fragments ahead of the columnar front are needed to provoke CET. Indeed, the CET occurs only when the fragments ahead of the columnar front block its growth. As concern modelling, this work could be transposed by the application of a higher probability of fragmentation in the dendrite competition regions showing a segregated region opened at the level of the solid-liquid interface to allow motion and transport of the fragments.

5. Conclusion

Al – 7 wt.% Si alloys directionally solidified in microgravity under purely diffusive conditions were analyzed in 3D using serial-sectioning. This technique is an effective way to characterize the dendrite orientations, shape, dimensions and to quantify the number of fragments in the studied volume. The discussion concerning the origin of the fragments was possible only because these experiments were performed in the absence of gravity effect which avoided their transport far from their detachment position.

The results show that when several dendrite orientations co-exist, more fragments are detached during solidification compared to the case of well-aligned dendrites. The dendrite growth competition, at incipient grain boundaries where dendrites with different orientations meet, can

lead to an accumulation of solute in the inter-dendritic liquid due the overlap of their respective solute layers. This enrichment in the solute concentration directly affects the morphology of the microstructure which is smaller, consistent with the observation of a lower volume-to-surface area ratio Sv^{-1} . All these conditions contribute to a higher fragmentation probability. Thus, it is clear that dendrite misorientation during solidification plays an important role in setting the number of fragments observed in castings and other solidification processes.

Acknowledgement

This research work is supported by the European Space Agency under the CETSOL (Columnar to Equiaxed Transition in SOLidification processes) ESA MAP project (AO-99-117), the French National Space Agency (CNES) and the German BMWi/DLR under FKZ 50WM1743 and FKZ 50WM2043. The authors acknowledge Hydro Aluminium Rolled Products GmbH for providing the alloys used in this paper.

References

- [1] Ch.-A. Gandin, Experimental Study of the Transition from Constrained to Unconstrained Growth during Directional Solidification., *ISIJ Int.* 40 (2000) 971–979. <https://doi.org/10.2355/isijinternational.40.971>.
- [2] L. Abou-Khalil, K.S. da Cruz, G. Reinhart, N. Mangelinck-Noël, H. Nguyen-Thi, Influence of growth velocity on fragmentation during directional solidification of Al – 14 wt.% Sn alloy studied by in-situ synchrotron X-radiography, *Acta Mater.* 241 (2022) 118370. <https://doi.org/10.1016/j.actamat.2022.118370>.
- [3] D. Ruvalcaba, R.H. Mathiesen, D.G. Eskin, L. Arnberg, L. Katgerman, In situ observations of dendritic fragmentation due to local solute-enrichment during directional solidification of an

- aluminum alloy, *Acta Mater.* 55 (2007) 4287–4292. <https://doi.org/10.1016/j.actamat.2007.03.030>.
- [4] M. Schwarz, A. Karma, K. Eckler, D.M. Herlach, Physical Mechanism of Grain Refinement in Solidification of Undercooled Melts, *Phys. Rev. Lett.* 73 (1994) 1380–1383. <https://doi.org/10.1103/PhysRevLett.73.1380>.
- [5] B. Li, H. Brody, A. Kazimirov, Real-time observation of dendrite coarsening in Sn-13%Bi alloy by synchrotron microradiography, *Phys. Rev. E.* 70 (2004) 062602. <https://doi.org/10.1103/PhysRevE.70.062602>.
- [6] G. Reinhart, H. Nguyen-Thi, N. Mangelinck-Noël, J. Baruchel, B. Billia, In Situ Investigation of Dendrite Deformation During Upward Solidification of Al-7wt.%Si, *JOM.* 66 (2014) 1408–1414. <https://doi.org/10.1007/s11837-014-1030-z>.
- [7] R.H. Mathiesen, L. Arnberg, P. Bleuet, A. Somogyi, Crystal fragmentation and columnar-to-equiaxed transitions in Al-Cu studied by synchrotron X-ray video microscopy, *Metall. Mater. Trans. A.* 37 (2006) 2515–2524. <https://doi.org/10.1007/BF02586224>.
- [8] B. Cai, J. Wang, A. Kao, K. Pericleous, A.B. Phillion, R.C. Atwood, P.D. Lee, 4D synchrotron X-ray tomographic quantification of the transition from cellular to dendrite growth during directional solidification, *Acta Mater.* 117 (2016) 160–169. <https://doi.org/10.1016/j.actamat.2016.07.002>.
- [9] C.J. Paradies, R.N. Smith, M.E. Glicksman, The influence of convection during solidification on fragmentation of the mushy zone of a model alloy, *Metall. Mater. Trans. A.* 28 (1997) 875–883. <https://doi.org/10.1007/s11661-997-0075-9>.
- [10] H.J. Jung, N. Mangelinck-Noël, H. Nguyen-Thi, N. Bergeon, B. Billia, A. Buffet, J. Baruchel, CET by Fragmentation during the Solidification under Natural and Forced Convection of Non-Refined Al-Based Alloys, *Mater. Sci. Forum.* 649 (2010) 343–348. <https://doi.org/10.4028/www.scientific.net/MSF.649.343>.
- [11] T. Campanella, C. Charbon, M. Rappaz, Grain refinement induced by electromagnetic stirring: A dendrite fragmentation criterion, *Metall. Mater. Trans. A.* 35 (2004) 3201–3210. <https://doi.org/10.1007/s11661-004-0064-1>.
- [12] Y.Z. Li, N. Mangelinck-Noël, G. Zimmermann, L. Sturz, H. Nguyen-Thi, Comparative study of directional solidification of Al-7 wt% Si alloys in Space and on Earth: Effects of gravity on dendrite growth and Columnar-to-equiaxed transition, *J. Cryst. Growth.* 513 (2019) 20–29. <https://doi.org/10.1016/j.jcrysgro.2019.02.050>.
- [13] D.R. Liu, N. Mangelinck-Noël, Ch.-A. Gandin, G. Zimmermann, L. Sturz, H. Nguyen-Thi, B. Billia, Simulation of directional solidification of refined Al-7 wt.%Si alloys – Comparison with benchmark microgravity experiments, *Acta Mater.* 93 (2015) 24–37. <https://doi.org/10.1016/j.actamat.2015.03.058>.
- [14] R.P. Mooney, L. Sturz, G. Zimmermann, N. Mangelinck-Noël, H. Nguyen-Thi, Y. Li, D.J. Browne, S. McFadden, Concurrent model for sharp and progressive columnar to equiaxed transitions validated by directional solidification experiments processed in microgravity conditions, *Comput. Mater. Sci.* 210 (2022) 111436. <https://doi.org/10.1016/j.commatsci.2022.111436>.
- [15] S. McFadden, R.P. Mooney, L. Sturz, G. Zimmermann, A Nucleation Progenitor Function approach to polycrystalline equiaxed solidification modelling with application to a microgravity transparent alloy experiment observed in-situ, *Acta Mater.* 148 (2018) 289–299. <https://doi.org/10.1016/j.actamat.2018.02.012>.

- [16] I. Steinbach, H.-J. Diepers, C. Beckermann, Transient growth and interaction of equiaxed dendrites, *J. Cryst. Growth.* 275 (2005) 624–638. <https://doi.org/10.1016/j.jcrysgro.2004.12.041>.
- [17] G. Salloum-Abou-Jaoude, H. Nguyen-Thi, G. Reinhart, R.H. Mathiesen, G. Zimmermann, D. Voss, Characterization of Motion of Dendrite Fragment by X-Ray Radiography on Earth and under Microgravity Environment, *Mater. Sci. Forum.* 790–791 (2014) 311–316. <https://doi.org/10.4028/www.scientific.net/MSF.790-791.311>.
- [18] Y.Z. Li, N. Mangelinck-Noël, G. Zimmermann, L. Sturz, H. Nguyen-Thi, Modification of the microstructure by rotating magnetic field during the solidification of Al-7 wt.% Si alloy under microgravity, *J. Alloys Compd.* 836 (2020) 155458. <https://doi.org/10.1016/j.jallcom.2020.155458>.
- [19] Y.Z. Li, N. Mangelinck-Noël, G. Zimmermann, L. Sturz, H. Nguyen-Thi, Effect of solidification conditions and surface pores on the microstructure and columnar-to-equiaxed transition in solidification under microgravity, *J. Alloys Compd.* 749 (2018) 344–354. <https://doi.org/10.1016/j.jallcom.2018.03.300>.
- [20] D.R. Liu, N. Mangelinck-Noël, Ch.-A. Gandin, G. Zimmermann, L. Sturz, H. Nguyen Thi, B. Billia, Structures in directionally solidified Al–7wt.% Si alloys: Benchmark experiments under microgravity, *Acta Mater.* 64 (2014) 253–265. <https://doi.org/10.1016/j.actamat.2013.10.038>.
- [21] L. Salvo, M. Suéry, A. Marmottant, N. Limodin, D. Bernard, 3D imaging in material science: Application of X-ray tomography, *Comptes Rendus Phys.* 11 (2010) 641–649. <https://doi.org/10.1016/j.crhy.2010.12.003>.
- [22] M. Becker, M. Kolbe, S. Steinbach, F. Kargl, Surface boundary-dendrite interactions in thin metallic Al-alloy samples, *Scr. Mater.* 209 (2022) 114386. <https://doi.org/10.1016/j.scriptamat.2021.114386>.
- [23] J. Alkemper, P.W. Voorhees, Quantitative serial sectioning analysis, *J. Microsc.* 201 (2001) 388–394. <https://doi.org/10.1046/j.1365-2818.2001.00832.x>.
- [24] J. Alkemper, P.W. Voorhees, Three-dimensional characterization of dendritic microstructures, *Acta Mater.* 49 (2001) 897–902. [https://doi.org/10.1016/S1359-6454\(00\)00355-4](https://doi.org/10.1016/S1359-6454(00)00355-4).
- [25] T. Cool, P.W. Voorhees, Dendrite fragmentation: an experiment-driven simulation, *Philos. Trans. R. Soc. Math. Phys. Eng. Sci.* 376 (2018) 20170213. <https://doi.org/10.1098/rsta.2017.0213>.
- [26] M.L. Comer, E.J. Delp, Parameter estimation and segmentation of noisy or textured images using the EM algorithm and MPM estimation, in: *Proc. 1st Int. Conf. Image Process., IEEE Comput. Soc. Press, Austin, TX, USA, 1994: pp. 650–654.* <https://doi.org/10.1109/ICIP.1994.413651>.
- [27] D.W. Kim, M.L. Comer, Channel detection in microscope images of materials using marked point process modeling, in: *2015 IEEE Int. Conf. Image Process. ICIP, IEEE, Quebec City, QC, Canada, 2015: pp. 3054–3058.* <https://doi.org/10.1109/ICIP.2015.7351364>.
- [28] C.A. Schneider, W.S. Rasband, K.W. Eliceiri, NIH Image to ImageJ: 25 years of image analysis, *Nat. Methods.* 9 (2012) 671–675. <https://doi.org/10.1038/nmeth.2089>.
- [29] H.J.G. Gundersen, Notes on the estimation of the numerical density of arbitrary profiles: the edge effect, *J. Microsc.* 111 (1977) 219–223. <https://doi.org/10.1111/j.1365-2818.1977.tb00062.x>.

- [30] T. Cool, P.W. Voorhees, The evolution of dendrites during coarsening: Fragmentation and morphology, *Acta Mater.* 127 (2017) 359–367. <https://doi.org/10.1016/j.actamat.2017.01.029>.
- [31] L.K. Aagesen, A.E. Johnson, J.L. Fife, P.W. Voorhees, M.J. Miksis, S.O. Poulsen, E.M. Lauridsen, F. Marone, M. Stampanoni, Universality and self-similarity in pinch-off of rods by bulk diffusion, *Nat. Phys.* 6 (2010) 796–800. <https://doi.org/10.1038/nphys1737>.
- [32] T. Takaki, S. Sakane, M. Ohno, Y. Shibuta, T. Shimokawabe, T. Aoki, Large-scale Phase-field Studies of Three-dimensional Dendrite Competitive Growth at the Converging Grain Boundary during Directional Solidification of a Bicrystal Binary Alloy, *ISIJ Int.* 56 (2016) 1427–1435. <https://doi.org/10.2355/isijinternational.ISIJINT-2016-156>.
- [33] M. Gündüz, E. Çadırlı, Directional solidification of aluminium–copper alloys, *Mater. Sci. Eng. A.* 327 (2002) 167–185. [https://doi.org/10.1016/S0921-5093\(01\)01649-5](https://doi.org/10.1016/S0921-5093(01)01649-5).
- [34] H. Neumann-Heyme, K. Eckert, C. Beckermann, Dendrite fragmentation in alloy solidification due to sidearm pinch-off, *Phys. Rev. E.* 92 (2015) 060401. <https://doi.org/10.1103/PhysRevE.92.060401>.